Nanofilament array embedded tungsten oxide for highly efficient electrochromic supercapacitor electrodes

Jongmin Kim,[a] Akbar I. Inamdar ,[a] Yongcheol Jo,[a] Sangeun Cho,[a] Abu Talha Aqueel Ahmed,[a] Bo Hou,[b] SeungNam Cha,[c] Tae Geun Kim,[d] Hyungsang Kim,[a] & Hyunsik Im*,[a]*

[a] *Division of Physics and Semiconductor Science, Dongguk University, Seoul 04620, South Korea*
[b] *Department of Engineering Science, University of Cambridge, Cambridge, CB2 1TN, UK*
[c] *Department of Physics, Sungkyunkwan University, Suwon, 16419, Republic of Korea*
[d] *Department of Electrical Engineering, Korea University, Seoul 02841, South Korea*

* Corresponding authors: hskim@dongguk.edu, hyunsik7@dongguk.edu

ABSTRACT: The high-activity of metallic nanofilament array (NFA) embedded tungsten oxide (WO_3) bifunctional electrodes for electrochromism and electrochemical energy storage is presented. The NFA reduces charge transfer resistance and increases the electrochemically active surface area at the electrode–electrolyte interface. The NFA-embedded WO_3 electrode exhibits a specific capacity of 214 F g^{-1} (pristine WO_3: 133 F g^{-1}) at 0.25 mA cm^{-2}, excellent cycling stability with ~92% capacitance retention after 2000 cycles (pristine WO_3: ~75% capacitance retention) and a coloration efficiency of 128 cm^2 C^{-1} (pristine WO_3: 91 cm^2 C^{-1}) with superb optical modulation. These properties are significantly more advanced compared to the pristine WO_3 electrode and superior to previously reported WO_3-based composites and nanostructured materials.

KEYWORDS: Nanofilament array; tungsten oxide; electrochromism; supercapacitor.

* **Corresponding authors**: hskim@dongguk.edu, hyunsik7@dongguk.edu

Since the concept of "nanoscience" was first introduced in the 1960s, nanomaterials and nanotechnologies have been rapidly applied in numerous industries and fundamental research fields. In particular, as both energy demand and consumption have increased tremendously in diverse fields ranging from heavy industry to transportation to portable electronic devices, nanoscience has been exploited not only to enhance the performance of various energy storage and harvesting devices but also to use energy sources efficiently.[1,2] Considerable efforts have been devoted to advancing renewable and clean technologies combined with many natural energy sources for energy storage and mobile power generation. Smart supercapacitors, also called electrochromic supercapacitors, represent an attractive technology that provides superior power density with additional electrochromic functionalities.[3-5] The electrode material is a key element of a smart supercapacitor and is the primary determiner of its ultimate performance.

Smart supercapacitors exploit electrochemical and electrochromic processes at the electrode–electrolyte interface and because these processes share a similar redox chemical reaction mechanism at the interface, the energy storage levels can be observed by monitoring the color of the active electrode. In general, a high-performance smart supercapacitor electrode exhibits the following attributes: a large electrochemically active surface area, high electrical conductivity, high ionic transport rate, and high electrochemical durability. The common technology strategy for developing high-performance electrodes is to fabricate hybrid composite materials whose constituting materials produce synergetic effects that enhance the four aforementioned attributes for improved performance.

Because of a high degree of color tailorability, state-of-the-art smart supercapacitors are fabricated using oxide/hydroxide-based materials which typically exhibit a high power density, fast charge/discharge rate, good safety, and long cycle life.[6-9] Among electrochromic oxide materials, tungsten oxide (WO_x, $x \approx 3$) has attracted widespread attention because of its fast color switching and high coloration efficiency.[10-12] In addition, WO_x composite films containing

additives, for example, Nb dopant ions,[13] lithium phosphorous oxynitride,[14] or reduced graphene oxide[15] have been investigated to improve electrochromic properties. On the contrary, pure bulk WO_x shows poor electrochemical performance and stability as a supercapacitor electrode. Numerous attempts to enhance its electrochemical activities through the development of hybrid composite materials such as WO_3/carbon aerogels,[16] polyaniline/WO_3,[17] WO_{3-x}/MoO_{3-x},[18] $WO_3/Ag/WO_3$,[19] and WO_3/TiO_2,[20] have been reported.

In the present work, we present a unique but generally applicable method to enhance both the electrochemical and electrochromic properties of a metal oxide-based smart supercapacitor electrode by embedding a nanoscale metallic nanofilament array (NFA), formed via an electroforming process, across a dielectric insulator electrode.[21-23] The NFA improves the electrochemical activity at the surface and the bulk electrical conductivity, substantially enhancing both the electrochromic and the electrochemical energy storage properties of the metal oxide.

Amorphous tungsten oxide (WO_3) thin-film electrodes were deposited onto indium tin oxide (ITO)-coated conducting glass substrates using a conventional radio frequency (RF) magnetron sputtering system with a pure tungsten oxide target. The thicknesses of the tungsten oxide films were measured using field-emission scanning electron microscopy (FE-SEM) and estimated to be ~250 nm (Fig. S1c). The actual chemical compositions of the $WO_{3+\square}$ films were determined by Rutherford backscattering spectroscopy (RBS) measurements, as shown in Fig. S1d. The $\square$ value was measured to be 0.191, indicating the presence of excess oxygen, which is associated with negative ion effects during sputtering.[24]

Fig. 1a is a schematic of a metallic NFA embedded in a WO_3 film. The array was fabricated by electroforming WO_3 using a parameter analyzer (Keithley 4200-SCS) with a two-probe system, where Au tips contacted the WO_3 film and the conducting ITO substrate. Moreover, the pristine WO_3 and NFA-embedded WO_3 films have a similar surface morphology

(Fig. S1a and b). When a positive voltage was applied, the leakage current also increased; however, beyond a critical voltage, the current abruptly increased (Fig. S4a). This phenomenon is known as "electroforming". After the electroforming process, the insulating WO_3 film showed reversible bi-stable resistance states between the high-resistance state (HRS) and the low-resistance state (LRS). Fig. 1b shows the measured resistive switching characteristics. This observed resistive switching behavior is typical of unipolar resistive switching.[25] The resistive switching points are spaced 500 μm apart while within the electrode area of 1 cm × 1 cm, 300 resistive switching points are formed. Fig. 1c shows the distribution of the measured resistance. The resistive switching mechanism is explained by the reversible creation and rupture of nanofilamentary paths via a redox chemical reaction (see Fig. S3 for more details).[26] The resistance retention characteristics of the LRS is evaluated at a constant readout voltage of 0.1 V. Fig. S4b shows the time-dependent current fluctuation in the LRS for the WO_3 electrode with an NFA at room temperature. The LRS retention is found to be very stable for over 30,000 s, demonstrating a non-volatile low-resistance behavior for enhanced charge transfer dynamics at the electrode–electrolyte interface.[27]

Fig. 1d and e show the X-ray photoelectron spectroscopy (XPS) spectra of the pristine (before electroforming) and NFA-embedded WO_3 electrodes surfaces, respectively. For the pristine WO_3 electrode, three binding-state peaks are observed at 33.5 eV, 34.2 eV, and 36.3 eV, which correspond to the W^{5+} and W^{6+} oxidation states. By contrast, the WO_3 with an NFA shows four binding-state peaks at approximately 30.1 eV (W^0), 32.2 eV (W^{4+}), 33.5 eV (W^{5+}), and 36.3 eV (W^{6+}).[28,29] Carbon (C) 1s photoelectrons with a binding energy of 285.0 eV were used for reference purposes.[30] After electroforming, the magnitude of the two major insulating binding states of W^{6+} and W^{5+} decreased; however, the metallic (or semiconducting and metallic) binding-state peaks of W^{4+} and W^0, which were not detected in the spectrum of the pristine WO_3 electrode, clearly appeared in the spectrum (Table S1). The existence of the

metallic binding state of W^0 suggests that metallic conducting channels are formed across the film, improving the electrical conductivity of the pristine WO_3 electrode.[31,32] Fig. S2 shows the O1s peak of the pristine WO_3 and NFA-embedded WO_3 films. The main peak can be deconvoluted into two peaks at 529.3 eV and 530.2 eV that correspond to the lattice oxygen and non-lattice oxygen, respectively. The amount of oxygen vacancies is proportional to the ratio of non-lattice oxygen. For the NFA-embedded WO_3 electrode, the percentage of non-lattice oxygen increases, indicating high-density oxygen vacancies in the film. The depth-profile XPS spectra taken from various resistive switching metal oxides that exhibit similar unipolar resistive switching behaviors confirm that metallic binding states are formed vertically across the bulk metal oxide film rather than only on the surface.[33] On the contrary, substantial changes in the binding states of W were not detected after LRS ↔ HRS switching, implying that the LRS ↔ HRS switching is determined by the microscopic chemical redox reaction in W–O binding states in the nanoscale region.[34,35]

Using transmission electron microscopy (TEM), we confirmed the existence of nanofilaments embedded in the WO_3. The presence of Moiré fringes explains the structural changes of the WO_3, indicating the formation of conducting nanofilamentary paths (Fig. 1f).[36] These superposed paralleled lattice planes, which induce Moiré fringes, originate from the rearrangement of oxygen vacancies during the electroforming process which result in different lattice spacing. Indeed, the high-resolution TEM (HR-TEM) image clearly shows interplanar spacings of 0.36 nm and 0.22 nm, which correspond to WO_3 and metallic W respectively (Fig. 1g). The observed microscopic structural changes in WO_3 are associated with the migration of oxygen ions under a high-voltage bias.[37] After the electroforming process, the selected-area

electron diffraction (SAED) pattern showed diffraction rings, demonstrating the polycrystalline nature of the prepared materials.[38,39] Furthermore, we resolve not only the (200), (202), (222), and (400) planes of the WO_3 phase but also the (110) plane of metallic W (Fig. S1e). Fig. 1h shows the conductive-AFM image used to investigate the local conductivity distribution of the WO_3 electrode. Conductive paths were observed after the electroforming process, indicating the formation of nanofilaments across the WO_3 film.[40]

The supercapacitor properties of the electrode materials were studied using cyclic voltammetry (CV). The CV curves of pristine WO_3 and NFA-embedded WO_3 were recorded at different scan rates ranging from 5 to 100 mV s^{-1} in a 1 M $LiClO_4$ + PC electrolyte between −0.9 and 0.5 V (vs. SCE), as shown in Fig. 2a and c. With increasing scan rate, the quasi-rectangular CV shape becomes deformed; this phenomenon is associated with the slow charge–discharge kinetics and diffusion limitation at the electrode–electrolyte interface.[41]

Fig. 2b and d show the stability tests for 2000 cycles at a scan rate of 100 mV s^{-1}. For the NFA-embedded WO_3 electrode, the observed area under the curve is larger and more stable than that obtained from the pristine WO_3 electrode; this difference is partly associated with the greatly improved bulk electrical conductivity caused by the metallic nanofilaments across the WO_3 film. The specific capacitance (C_s) of the WO_3 electrodes can be calculated from the area under the CV curve using the following equation:[42,43]

$$C_s = \frac{1}{2\nu m \Delta V} \int I dV \quad (1)$$

where v is the scan rate (mV s^{-1}), m is the mass of the electrode film (g), ΔV is the potential window, and IdV is the area under the CV curve. Fig. 2e shows the specific capacitance of the pristine WO_3 and NFA-embedded WO_3 electrodes as a function of scan rate v. For both electrodes, the calculated specific capacitance increases gradually with decreasing scan rate, which is attributed to the facile diffusion of the electrolytic ions at low scan rates.[44,45]Furthermore, the NFA-embedded WO_3 electrode shows a substantially improved specific capacitance compared to the pristine WO_3 electrode at the same scan rate. In particular, the maximum specific capacitance of the pristine WO_3 and NFA-embedded WO_3 electrodes is 139 and 202 F g^{-1} at 5 mV s^{-1}, respectively. Most surprisingly, the NFA-embedded WO_3 electrode exhibits superior long-term cycling performance. Fig. 2f shows the measured cycling stability of the pristine WO_3 and NFA-embedded WO_3 electrodes for up to 2000 cycles at a scan rate of 100 mV s^{-1}. The pristine WO3 electrode shows ~75% capacitance retention after 2000 cycles, whereas the NFA-embedded WO3 electrode exhibits excellent long-term cycling stability with ~92% retention of its initial specific capacitance. In addition, the cycle performance for the pristine WO3 and NFA-embedded WO3 electrodes was measured up to 10000 cycles at an increased scan rate of 150 mV s^{-1} (Fig. S4c). It was found that the NFA- embedded WO3 electrode is more stable (~96%) than the pristine WO3 electrode (~89%). These results suggest that the NFA-embedded WO3 electrode can significantly enhance cycling performance because the conducting nanofilamentary paths serve as conductive networks that enable efficient electron transport during long-term cycling.

The CV data also provide the kinetics of the electrode reaction at various sweep rates according to the following equation:[46]

$$i = av^b \quad (2)$$

where *a* is a constant, *i* is the measured anodic peak current, and *v* is the scan rate. The value of parameter *b* can be determined from the slope of the log(*v*)–log(*i*) plot. A *b* value of 0.5 indicates that the redox process is controlled by a diffusion process, whereas a value of 1.0 indicates a surface-capacitive controlled process.[47] As shown in Fig. S4d, the calculated *b* value of the peakanodic current is between 0.5 and 1, indicating that both a surface capacitive effect and Li^+ intercalation reaction contribute to the measured current.

To further quantitatively analyze the pseudocapacitive contribution, we further model the reaction kinetics using the following equation:[48]

$$i(V) = k_1 V + k_2 V^{\frac{1}{2}} \quad (3)$$

where $i(V)$ is the current response at a fixed potential, v is the scan rate, and k_1 and k_2 are adjustable values. Fig. 3a shows plots of $i/v^{1/2}$ versus $v^{1/2}$ for the pristine WO_3 and NFA-embedded WO_3 electrodes at 0.1 V. By calculating both k_1 and k_2, we could distinguish the contribution ratio of the capacitive effects (k_1v) and the diffusion-controlled insertions ($k_2v^{1/2}$) at specific potentials. Fig. 3b shows the calculated contribution ratio at various scan rates for the electrodes. These results reveal that the percentage of capacitive contributions increases with increasing scan rate. For the pristine WO_3 electrode, as the scan rate increases the redox reaction at the surface is also enhanced, increasing the capacitive effect. In addition, the capacitive contribution of the NFA-embedded WO_3 electrode is greater than that of the pristine WO_3 electrode at all scan rates. This is because electroforming-induced negatively charged oxygen ions on the electrode surface can enhance the absorption of Li^+ at the electrode/electrode interface. Fig. 3c–f show the capacitive contributions (the shaded region) at both 5 and 80 mV s^{-1}. The larger capacitive contribution value of the NFA-embedded WO_3 electrode suggests that it participates in a fast redox reaction during the electrochemical process.[49] The fast redox reaction of the NFA-embedded WO_3 electrode is associated with fast electron transfer kinetics, which provides excellent pseudocapacitive properties.

The accessible electrochemical reaction surface area can be estimated by analyzing the electrochemically active surface area (ECSA). Fig. 4a and b show the CV curves of the pristine WO_3 and the NFA-embedded WO_3 electrodes in the non-faradaic region. The scan rate (v)-dependent capacitive current (I_{DL}) is obtained from the non-faradaic region as follows:[50]

$$I_{DL} = C_{DL} \times v \quad (4)$$

where C_{DL} is the double-layer region-specific capacitance that corresponds to the slope of the I_{DL} characteristics. Fig. 4c shows the I_{DL} at 0.3 V. The ECSA of the electrode was calculated according to the equation:[51]

$$ECSA = C_{DL}/C_S \quad (5)$$

where C_s (0.035 mF cm^{-2} for H_2SO_4) is the specific capacitance of the electrolyte. The

calculated ECSA value for the pristine WO_3 and NFA-embedded WO_3 electrodes is 10.1 and 71.7 cm^2, respectively. The observed higher ECSA value for the NFA-embedded WO_3 electrode suggests that electroforming-induced low-oxygen (WO_x, $0 < x < 3$) surface chemical states are naturally favorable to electrochemical reactions and activity.[52]

We investigated the charge–discharge dynamics of the electrodes by measuring their galvanostatic charge–discharge (GCD) characteristics at various current densities (0.25–1 mA cm^{-2}). The potential window was fixed from −0.9 to 0.45 V (vs. SCE). Fig. 5a and b show the recorded charge–discharge curves, which exhibit typical pseudocapacitive behaviors, confirming that faradaic reactions are responsible for the charge storage.[53] The specific capacitance of the electrodes can be calculated using their galvanostatic discharge curves by the following equation:[54]

$$C_s = \frac{I\Delta t}{m\Delta V} \quad (6)$$

where I is the response current and Δt represents the discharge time. Fig. 5c presents the calculated specific capacitance of the electrodes at different current densities. The decrease of specific capacitance with increasing current density is due to the poor penetration and diffusion

of the electrolyte.[55] The maximum specific capacitance for the pristine WO_3 and NFA-embedded WO_3 electrodes is 133 and 214 F g^{-1} at 0.25 mA cm^{-2}, respectively. The obtained specific capacitance of the NFA-embedded WO_3 electrode is much higher than that of the pristine WO_3 electrode by ~ 61%. The coulombic efficiencies (η) of all the electrodes exhibit ~99% at various current densities. There is a slight variation in the specific capacitance from the CV and GCD curves. This is because the specific capacitance obtained by CV is calculated at a particular potential, while that obtained from the GCD is an average capacitance over the potential range.[56]

From the galvanostatic charge–discharge curves, the gravimetric energy density (*E*) and power density (*P*) can be calculated from the following formulas:[57,58]

$$E = \frac{1}{2} C_s \Delta V^2 \quad (7)$$

$$P = \frac{E}{\Delta t} \quad (8)$$

where ΔV is the voltage range and Δt is the discharge time. Fig. 5d presents the calculated power density as a function of energy density (Ragone plot) and it can be seen that the NFA-embedded WO_3 electrode shows higher energy and power densities compared to the pristine WO_3 electrode. To further evaluate the electrochemical energy storage performance of the electrodes, asymmetric supercapacitors were assembled using the WO_3 electrode as a positive electrode and carbon (C) as a negative electrode (Fig. S5a). The asymmetric supercapacitor devices were tested in a two-electrode cell with a 1 M $LiClO_4$ + PC

electrolyte. The total amount of charge (Q) stored in each positive and negative electrode must be equal and it is given by the following equations:

$$Q_+ = Q_- \tag{9}$$

$$(m_+) \times (i_+) \times \Delta t_+ = (m_-) \times (i_-) \times \Delta t \tag{10}$$

where m represents the loading mass, i indicates the delivered current, and Δt is the discharge time of the individual electrodes. The + and – signs are used in the subscript to denote the positive and negative electrodes, respectively. The charge/discharge curves were recorded in a wide potential window range between -0.9 and 0.45 V. Fig. S5b and c show the charge–discharge profiles of the pristine WO3//C and NFA- embedded WO3//C asymmetric devices. Clearly, the NFA-embedded WO3//C device shows a longer discharge time compared to the pristine WO3//C asymmetric device. The obtained results were plotted in the Ragone plot, as shown in Fig. S6. The NFA- embedded WO3//C asymmetric supercapacitor shows higher energy and power densities than the pristine WO3//C device.

We further investigated changes in the interfacial properties of the electrodes after long-term stability testing using EIS analysis in the frequency range from 10 kHz to 0.1 Hz. Fig. 5e and f show the Nyquist plots of the pristine WO_3 and NFA-embedded WO_3 electrodes before

and after 2000 CV cycles at a scan rate of 100 mV s^{-1}. The equivalent circuit is shown as an inset in Fig. 5f. *CPE* represents the constant phase element. The intercept of the real impedance (Z_{re}) in the high-frequency region of the Nyquist plot corresponds to the solution resistance (R_s), which includes both the internal resistance of the electrode and the bulk resistance of the electrolyte.[59] The charge transfer resistance (R_{ct}) can be obtained directly from the diameter of the semicircle in the high-frequency region.[60,61] The slope of a straight line in the low-frequency region corresponds to the Warburg impedance (Z_w) which is related to the diffusion of Li^+ ions into the electrode.[62,63] Fitted values for the main circuit parameters are listed in Table 1 and it can be seen that the R_s of the NFA-embedded WO_3 electrode is smaller than that of the pristine WO_3 electrode, which due to the enhanced conductivity associated with the conducting NFA. Furthermore, the EIS spectrum of the NFA-embedded WO_3 electrode exhibits almost no semicircle; its theoretically modelled R_{ct} value is 5.5 Ω, indicating very fast charge transfer between the electrode and the electrolyte. Before cycling, the NFA-embedded WO_3 electrode exhibited a large Z_w value because of the oxygen-ion migration in the electroforming process.[64,65] In particular, the R_s, R_{ct}, and Z_w values of the pristine WO_3 electrode are much higher than those obtained for the NFA-embedded WO_3 electrode after 2000 cycles, explaining the observed low specific capacitance and poor stability of the pristine WO_3 electrode.[66]

The WO_3 material shows a favorable and reversible color change between transparent and blue. Compared with other electrochromic metal oxide materials, WO_3 exhibits a superior coloration efficiency (CE) and electrochromic response time.[67] The electrochromic process depends on the intercalation/deintercalation of Li^+ ions into/from the WO_3 electrode near the surface. The reaction mechanism can be represented as:[68]

$$WO_3 + xLi^+ + xe^- \ (\text{discharged/transparent}) \leftrightarrow Li_xWO_3 \ (\text{charged/blue}) \quad (11)$$

During the cathodic potential scan, the intercalation of Li^+ ions induces the reduction of the W^{6+} state to the W^{5+} state, resulting in the electrochromic effect (blue coloration of the film).[69,70] By contrast, during the anodic potential scan, an oxidation reaction at the electrode–electrolyte interface causes deintercalation of Li^+ ions from the W^{5+} state to the W^{6+} state, making the electrode transparent (bleached). To evaluate the electrochromic properties of both the pristine WO_3 and NFA-embedded WO_3 electrodes, we conducted optical transmittance measurements by applying potential steps of ±0.75 V (vs. SCE) for a fixed time of 30 s. The transmittance spectra for the electrodes were recorded in the colored and bleached states, as shown in Fig. 6a and b. The optical density (ΔOD) was estimated at 630 nm using the following equation:

$$(\Delta OD) = \log\left(\frac{T_b}{T_c}\right) \quad (12)$$

where T_b and T_c are the transmittance at the bleached and colored states, respectively. The optical modulation for the pristine WO_3 and NFA-embedded WO_3 electrodes is found to be approximately 55% and 67%, respectively (Fig. S7a and b).

Fig. 6c and d show the chronocoulometry curves used to investigate the amount of intercalated (Q_i) and deintercalated charge (Q_{di}). The electrochromic reversibility ($\Re$) was calculated according to the following equation:[71]

$$\Re(\%) = \frac{Q_{di}}{Q_i} \times 100 \quad (1\,\Re)$$

After electroforming, the electrochromic reversibility of the WO_3 electrode increases considerably from 30 to 37%. The improved reversibility is associated with the electroforming

induced favorable surface states for the intercalation/deintercalation processes and is consistent with the enhanced electrochemical energy storage performance. The coloration efficiency is critical to electrochromic performance and can be calculated as:[72]

$$CE = (\Delta OD)/Q/A \quad (14)$$

where *Q*/*A* represents the amount of charge per unit area of the electrode's surface. The WO_3 electrode with NFA exhibits a remarkably improved CE of 128 $cm^2\ C^{-1}$ compared to that obtained for the pristine WO_3 of 91 $cm^2\ C^{-1}$ (Fig. S7c). The observed electrochromic performance is summarized in Table 2. As shown in Fig. 6e and f, the NFA-embedded WO_3 electrode, with superior CE, exhibits a darker blue color in the colored state at − 0.75 V.

In this work, we fabricated a tungsten oxide film electrode in which an electroforming-induced metallic NFA was embedded, and subsequently investigated its smart supercapacitor properties. The NFA-embedded WO_3 electrode demonstrated superior specific capacitance, long-term cycling stability, and CE compared to the pristine WO_3 electrode. This performance improvement is due to the synergetic effects between its enhanced bulk conductivity, increased electrochemically active surface area, and fast charge transfer kinetics. Our experimental findings could pave the way for a new powerful concept for smart supercapacitor applications and can further be extended to improve other electrodes for water electrolysis and batteries.

Experimental section

Electrode fabrication: We fabricated WO_3 electrode films using RF magnetron sputtering with a WO_3 target (99.99% purity). Before deposition, ITO-coated glass substrates were ultrasonically cleaned with acetone, methanol, and deionized water (10 min each) and then dried with N_2 gas. The chamber was initially evacuated to 3.0×10^{-6} Torr and maintained at 10 mTorr. During the process of deposition, an Ar/O_2 gas flow mixture ratio was maintained at 8:2 with a sputtering power of 120 W for 20 min. The area of the electrode film was 1×1 cm^2 for electrochemical supercapacitor measurements and 2×2 cm^2 for electrochromic measurements.

Preparation of electrolyte: The electrolyte was prepared by mixing lithium perchlorate ($LiClO_4$) and propylene carbonate (PC) at room temperature. The $LiClO_4$ (5.315 g) was dissolved in 50 mL of PC using a magnetic stirrer for 10 min.

Material characterization: The thickness of a WO_3 electrode film was determined using field-emission scanning electron microscopy (FE-SEM, Hitachi S-4800). To investigate the microscopic structural properties of WO_3 electrode films, high-resolution transmission electron microscopy (HR-TEM, JEOL, JEM-3000F) analysis was employed. The chemical binding states were studied using X-ray photoelectron spectroscopy (XPS, PHI 5000 VersaProbe II, ULVAC-PHI, Inc., Japan). The transmittance spectra were collected using visible and near-infrared (VIS–NIR) spectroscopy (Tec5, Germany).

Electrical characterization: An NFA was formed across the WO_3 electrode film via electroforming using a Keithley 4200-SCS semiconductor characterization system with two-probe electrical measurements. The diameter of the probe tip used in the experiments was 10 μm.

Evaluation of the electrochemical and electrochromic performances: The electrochemical and electrochromic measurements were carried out using a potentiostat (Princeton Applied Research, VersaSTAT 3) with a standard three-electrode cell system in 1 M $LiClO_4$ + PC

electrolyte. The WO_3 electrodes were the working electrode. A saturated calomel electrode (SCE) and graphite were used as the reference electrode and counter electrode, respectively.

Acknowledgements

The authors would like to thank the financial support from the National Research Foundation (NRF) of Korea (Grant nos. 2016R1A3B1908249, 2016R1A6A1A03012877, 2018R1D1A1B07049046, 2018R1D1A1A09083859).

References

[1] Y.-Y. Liu, S.-H. Luo, S.-X. Yan, J. Feng and T.-F. Yi, *Ionics*, 2020, **26**, 415.

[2] S.-X. Yan, S.-H. Luo, J. Feng, P.-W. Li, R. Guo, Q. Wang, Y.-H. Zhang, Y.-G. Liu and S. Bao, *Chem. Eng. J*., 2020, **381**, 122695.

[3] J. Yan, S. Li, B. Lan, Y. Wu and P. S. Lee, *Adv. Funct. Mater*., 2020, **30**, 1902564.

[4] X. Chen, H. Lin, P. Chen, G. Guan, J. Deng and H. Peng, *Adv. Mater*., 2014, **26**, 4444.

[5] Y. Tian, S. Cong, W. Su, H. Chen, Q. Li, F. Geng and Z. Zhao, *Nano Lett*., 2014, **14**, 2150. [6] Y. Tian, W. Zhang, S. Cong, Y. Zheng, F. Geng and Z. Zhao, *Adv. Funct. Mater*., 2015, **25**, 5833.

[7] T. Deng, W. Zhang, O. Arcelus, J.-G. Kim, J. Carrasco, S. J. Yoo, W. Zheng, J. Wang, H. Tian, H. Zhang, X. Cui and T. Rojo, *Nat. Commun*., 2017, **8**, 15194.

[8] Y. Xu, Z. Lin, X. Zhong, X. Huang, N. O. Weiss, Y. Huang and X. Duan, *Nat. Commun*., 2014, **5**, 4554.

[9] J. Kim, H. Ju, A. I. Inamdar, Y. Jo, J. Han, H. Kim and H. Im, *Energy*, 2014, **70**, 473.

[10] J.-W. Liu, J. Zheng, J.-L. Wang, J. Xu, H.-H. Li and S.-H. Yu, *Nano Lett*., 2013, **13**, 3589.

[11] G. A. Niklasson and C. G. Granqvist, *J. Mater. Chem*., 2007, **17**, 127.

[12] A. I. Inamdar, J. Kim, Y. Jo, H. Woo, S. Cho, S. M. Pawar, S. Lee, J. L. Gunjakar, Y. Cho, B. Hou, S. Cha, J. Kwak, Y. Park, H. Kim and H. Im, *Sol. Energy Mater. Sol. Cells*, 2017, **166**, 78.

[13] S. R. Bathe and P. S. Patil, *J. Phys. D: Appl. Phys*., 2007, **40**, 7423.

[14] S. J. Yoo, J. W. Lim and Y.-E. Sung, *Sol. Energy Mater. Sol. Cells*, 2006, **90**, 477. [15] M. Zhi, W. Huang, Q. Shi, M. Wang and Q. Wang, *RSC Adv*., 2016, **6**, 67488. [16] Y.-H. Wang, C.-C. Wang, W.-Y. Cheng and S.-Y. Lu, *Carbon*, 2014, **69**, 287.

[17] H. Wei, X. Yan, S. Wu, Z. Luo, S. Wei and Z. Guo, *J. Phys. Chem. C*, 2012, **116**, 25052.

[18] X. Xiao, T. Ding, L. Yuan, Y. Shen, Q. Zhong, X. Zhang, Y. Cao, B. Hu, T. Zhai, L. Gong, J.Chen, Y. Tong, J. Zhou and Z. L. Wang, *Adv. Energy Mater*., 2012, **2**, 1328.

[19] H. Li, Y. Lv, X. Zhang, X. Wang and X. Liu, *Sol. Energy Mater. Sol. Cells*, 2015, **136**, 86.

[20] B. Pal, B. L. Vijayan, S. G. Krishnan, M. Harilal, W. J. Basirun, A. Lowe, M. M. Yusoff and R. Jose, *J. Alloy. Compd*., 2018, **740**, 703.

[21] A. Sawa, *Mater. Today*, 2008, **11**, 28.

[22] K. M. Kim, S. J. Song, G. H. Kim, J. Y. Seok, M. H. Lee, J. H. Yoon, J. Park and C. S. Hwang, *Adv. Funct. Mater*., 2011, **21**, 1587.

[23] J. Kim, K. Jung, Y. Kim, Y. Jo, S. Cho, H. Woo, S. Lee, A. I. Inamdar, J. Hong, J.-K. Lee, H. Kim and H. Im, *Sci. Rep*., 2016, **6**, 23930.

[24] J. Kim, A. I. Inamdar, Y. Jo, H. Woo, S. Cho, S. M. Pawar, H. Kim and H. Im, *ACS Appl. Mater. Interfaces*, 2016, **8**, 9499.

[25] J. A. Koza, E. W. Bohannan and J. A. Switzer, *ACS Nano*, 2013, **7**, 9940.

[26] Y. Jo, K. Jung, J. Kim, H. Woo, J. Han, H. Kim, J. Hong, J.-K. Lee and H. Im, *Sci. Rep*., 2014, **4**, 7354.

[27] H. Akinaga and H. Shima, *Proc. IEEE*, 2010, **98**, 2237.

[28] B. Liu, Y. Ma, A. Zhang, L. Chen, A. N. Abbas, Y. Liu, C. Shen, H. Wan and C. Zhou, *ACS Nano*, 2016, **10**, 5153.

[29] J. Ding, Y. Chai, Q. Liu, X. Liu, J. Ren and W.-L. Dai, *J. Phys. Chem. C*, 2016, **120**, 4345.

[30] D. Briggs and M. P. Seah, *Auger and X-ray Photoelectron Spectroscopy: Practical Surface Analysis*, Wiley, New York, 1990.

[31] M. Moors, K. K. Adepalli, Q. Lu, A. Wedig, C. Bäumer, K. Skaja, B. Arndt, H. L. Tuller, Dittmann, R. Waser, B. Yildiz and I. Valov, *ACS Nano*, 2016, **10**, 1481.

[32] J. Li, C. Aron, G. Kotliar and J. E. Han, *Nano Lett*., 2017, **17**, 2994.

[33] J. Choi, J. Song, K. Jung, Y. Kim, H. Im, W. Jung, H. Kim, Y. H. Do, J. S. Kwak and J. Hong, *Nanotechnology*, 2009, **20**, 175704.

[34] K. Jung, Y. Kim, Y. S. Park, W. Jung, J. Choi, B. Park, H. Kim, W. Kim, J. Hong and H. Im, *J. Appl. Phys*., 2011, **109**, 054511.

[35] S. Munjal and N. Khare, *Sci. Rep*., 2017, **7**, 12427.

[36] K. Baek, S. Park, J. Park, Y.-M. Kim, H. Hwang and S. H. Oh, *Nanoscale*, 2017, **9**, 582.

[37] D.-H. Kwon, K. M. Kim, J. H. Jang, J. M. Jeon, M. H. Lee, G. H. Kim, X.-S. Li, G.-S. Park, B. Lee, S. Han, M. Kim and C. S. Hwang, *Nature Nanotech*., 2010, **5**, 148.

[38] B. Hou, D. Parker, G. P. Kissling, J. A. Jones, D. Cherns and D. J. Fermín, *J. Phys. Chem. C*, 2013, **117**, 6814.

[39] N. Kattan, B. Hou, D. J. Fermín and D. Cherns, *Appl. Mater. Today*, 2015, **1**, 52.

[40] Y. Ren, V. Milo, Z. Wang, H. Xu, D. Ielmini, X. Zhao and Y. Liu, *Adv. Theory Simul*., 2018, **1**, 1700035.

[41] Y. Huang, M. Zhong, Y. Huang, M. Zhu, Z. Pei, Z. Wang, Q. Xue, X. Xie and C. Zhi, *Nat. Commun*., 2015, **6**, 10310.

[42] V. Kannan, A. I. Inamdar, S. M. Pawar, H.-S. Kim, H.-C. Park, H. Kim, H. Im and Y. S. Chae, *ACS Appl. Mater. Interfaces*, 2016, **8**, 17220.

[43] S. Cho, J. Kim, Y. Jo, A. T. A. Ahmed, H. S. Chavan, H. Woo, A. I. Inamdar, J. L. Gunjakar, R. M. Pawar, Y. Park, H. Kim and H. Im, *J. Alloy. Compd*., 2017, **725**, 108.

[44] H. B. Li, M. H. Yu, F. X. Wang, P. Liu, Y. Liang, J. Xiao, C. X. Wang, Y. X. Tong and G. W. Yang, *Nat. Commun*., 2013, **4**, 1894.

[45] S. M. Pawar, J. Kim, A. I. Inamdar, H. Woo, Y. Jo, B. S. Pawar, S. Cho, H. Kim and H. Im, *Sci. Rep*., 2016, **6**, 21310.

[46] C. Song, J. Yun, H. Lee, H. Park, Y. R. Jeong, G. Lee, M. S. Kim and J. S. Ha, *Adv. Funct. Mater*., 2019, **29**, 1901996.

[47] G. Zou, J. Guo, X. Liu, Q. Zhang, G. Huang, C. Fernandez and Q. Peng, *Adv. Energy Mater*., 2017, **7**, 1700700.

[48] Y. Han, Y. Lu, S. Shen, Y. Zhong, S. Liu, X. Xia, Y. Tong and X. Lu, *Adv. Funct. Mater*., 2019, **29**, 1806329.

[49] Y. Lan, H. Zhao, Y. Zong, X. Li, Y. Sun, J. Feng, Y. Wang, X. Zheng and Y. Du, *Nanoscale*, 2018, **10**, 11775.

[50] H. S. Chavan, B. Hou, A. T. A. Ahmed, Y. Jo, S. Cho, J. Kim, S. M. Pawar, S. Cha, A. I. Inamdar, H. Im and H. Kim, *Sol. Energy Mater. Sol. Cells*, 2018, **185**, 166.

[51] H. S. Chavan, B. Hou, A. T. A. Ahmed, J. Kim, Y. Jo, S. Cho, Y. Park, S. M. Pawar, A. I. Inamdar, S. N. Cha, H. Kim and H. Im, *J. Alloy. Compd*., 2018, **767**, 782.

[52] Z. Chen, M. Zhao, X. Lv, K. Zhou, X. Jiang, X. Ren and X. Mei, *Sci. Rep*., 2018, **8**, 30.

[53] A. I. Inamdar, Y. Jo, J. Kim, J. Han, S. M. Pawar, R. S. Kalubarme, C. J. Park, J. P. Hong, Y. S. Park, W. Jung, H. Kim and H. Im, *Energy*, 2015, **83**, 532.

[54] L.-Q. Mai, A. Minhas-Khan, X. Tian, K. M. Hercule, Y.-L. Zhao, X. Lin and X. Xu, *Nat. Commun*., 2013, **4**, 2923.

[55] R. R. Salunkhe, J. Lin, V. Malgras, S. X. Dou, J. H. Kim and Y. Yamauchi, *Nano Energy*, 2015, **11**, 211.

[56] E. Elanthamilan, S. Rajkumar, R. Rajavalli and J. P. Merlin, *New J. Chem*., 2018, **42**, 10300.

[57] P. A. Shinde, Y. Seo, C. Ray and S. C. Jun, *Electrochim. Acta*, 2019, **308**, 231.

[58] F. Han, G. Meng, F. Zhou, L. Song, X. Li, X. Hu, X. Zhu, B. Wu and B. Wei, *Sci. Adv*., 2015, **1**, e1500605.

[59] W. Wang, S. Guo, I. Lee, K. Ahmed, J. Zhong, Z. Favors, F. Zaera, M. Ozkan and C. S. Ozkan, *Sci. Rep*., 2014, **4**, 4452.

[60] S. H. Aboutalebi, A. T. Chidembo, M. Salari, K. Konstantinov, D. Wexler, H. K. Liu and S. X. Dou, *Energy Environ. Sci*., 2011, **4**, 1855.

[61] Y. Liu, Z. Wang, Y. Zhong, M. Tade, W. Zhou and Z. Shao, *Adv. Funct. Mater*., 2017, **27**, 1701229.

[62] Q. Lv, S. Wang, H. Sun, J. Luo, J. Xiao, J. Xiao, F. Xiao and S. Wang, *Nano Lett*., 2016, **16**, 40.

[63] X. Peng, H. Liu, Q. Yin, J. Wu, P. Chen, G. Zhang, G. Liu, C. Wu and Y. Xie, *Nat. Commun.*, 2016, **7**, 11782.

[64] K. Jung, H. Seo, Y. Kim, H. Im, J. Hong, J.-W. Park and J.-K. Lee, *Appl. Phys. Lett*., 2007, **90**, 052104.

[65] J. Kim, D. Kim, Y. Jo, J. Han, H. Woo, H. Kim, K. K. Kim, J. P. Hong and H. Im, *Thin Solid Films*, 2015, **589**, 188.

[66] A. T. A. Ahmed, H. S. Chavan, Y. Jo, S. Cho, J. Kim, S. M. Pawar, J. L. Gunjakar, A. I. Inamdar, H. Kim and H. Im, *J. Alloys Compd*., 2017, **724**, 744.

[67] Y. Li, W. A. McMaster, H. Wei, D. Chen and R. A. Caruso, *ACS Appl. Nano Mater*., 2018, **1**, 2552.

[68] H. Wei, X. Yan, Q. Wang, S. Wu, Y. Mao, Z. Luo, H. Chen, L. Sun, S. Wei and Z. Guo, *Energy Environ. Focus*, 2013, **2**, 112.

[69] F. Zheng, W. Man, M. Guo, M. Zhang and Q. Zhen, *CrystEngComm*., 2015, **17**, 5440.

[70] M. V. Limaye, J. S. Chen, S. B. Singh, Y. C. Shao, Y. F. Wang, C. W. Pao, H. M. Tsai, J. F. Lee, H. J. Lin, J. W. Chiou, M. C. Yang, W. T. Wu, J. S. Chen, J. J. Wu, M. H. Tsai and W. F. Pong, *RSC Adv*., 2014, **4**, 5036.

[71] A. J. More, R. S. Patil, D. S. Dalavi, S. S. Mali, C. K. Hong, M. G. Gang, J. H. Kim and P. S. Patil, *Mater. Lett*., 2014, **134**, 298.

[72] G. Cai, X. Wang, M. Cui, P. Darmawan, J. Wang, A. L.-S. Eh and P. S. Lee, *Nano Energy*, 2015, **12**, 258.

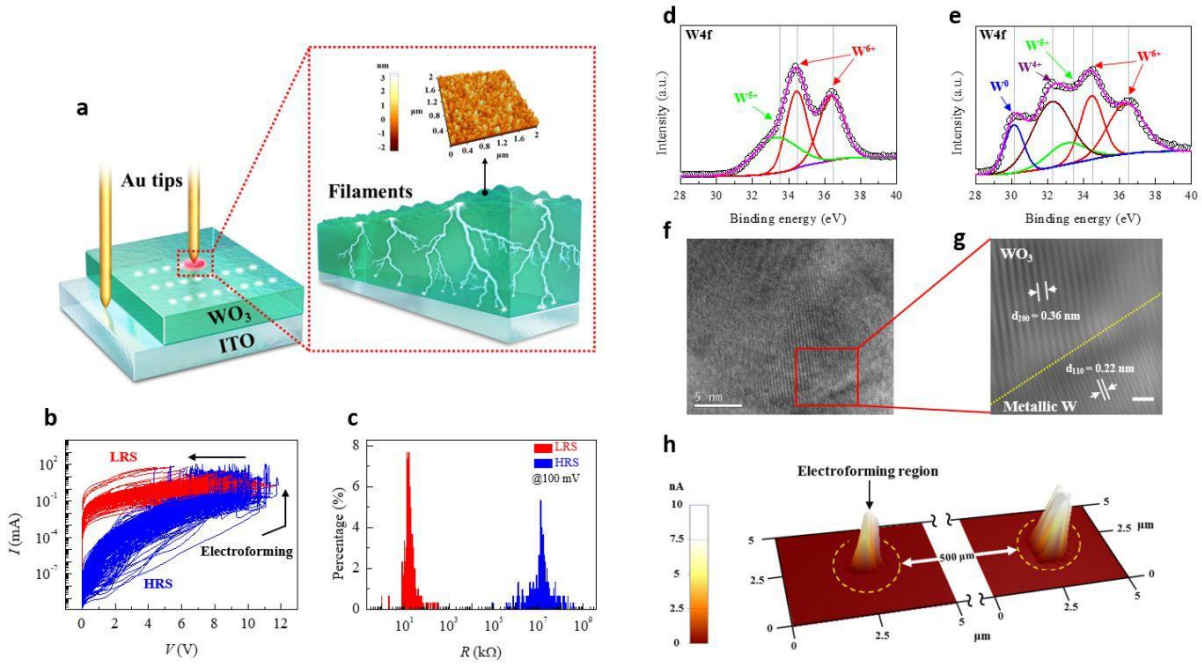

Fig. 1 (a) Schematic showing the formation of a conducting nanofilament array (NFA) across a WO_3 electrode film via an electroforming process. (b) Resistance-switching current–voltage (*I*–*V*) curves of the WO_3 film showing bi-stable resistance states. (c) The resistance distribution of the low- and high-resistance states extracted at a 0.1 V read voltage. XPS spectra of (d) the pristine WO_3 and (e) NFA-embedded WO_3 films. (f) Cross-sectional high-resolution TEM image of the NFA-embedded WO_3 film and (g) a magnified view showing the Moiré fringes. (h) Conductive-AFM image of the NFA-embedded WO_3 electrode measured with a compliance current of 10 nA.

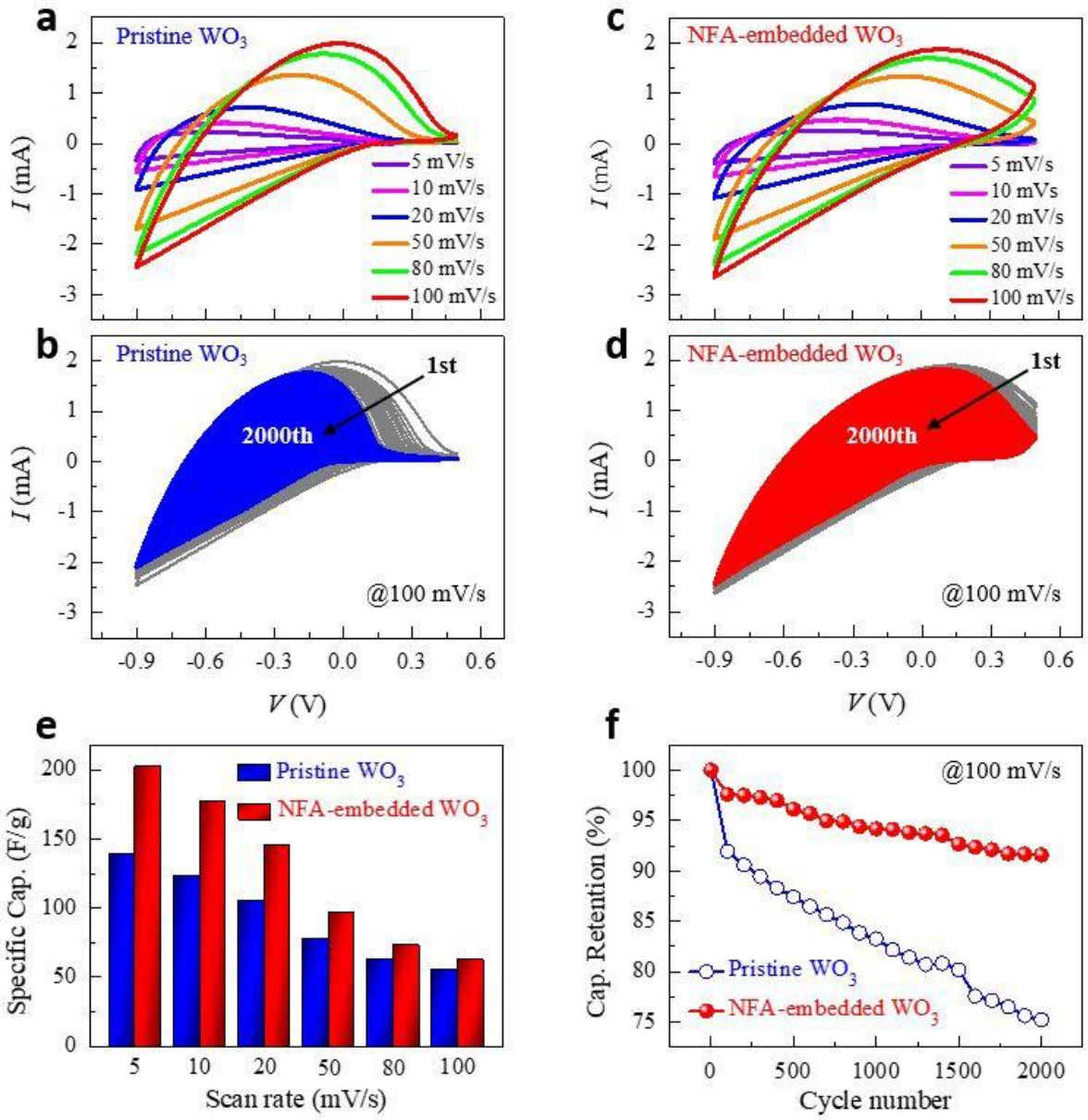

Fig. 2 (a, c) CV curves at various scan rates from 5 to 100 mV s^{-1} and (b, d) after 2000 continuous cycles at a scan rate of 100 mV s^{-1} for the pristine WO_3 and NFA-embedded WO_3 electrodes. (e) Comparison of the specific capacitance measured at different scan rates. (f) Long-term cycling stability of the pristine WO_3 and NFA-embedded WO_3 electrodes at a scan rate of 100 mV s^{-1}.

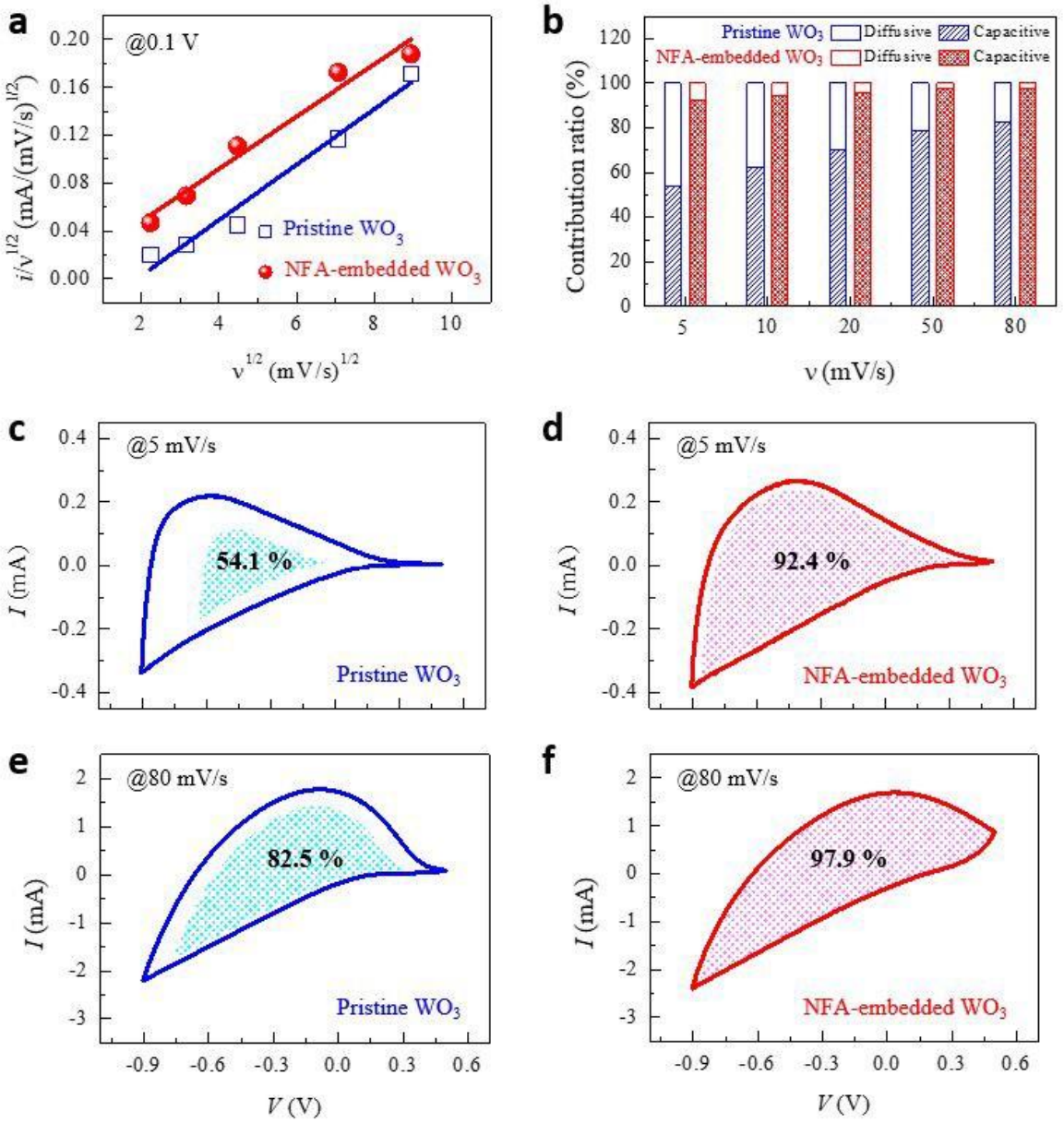

Fig. 3 (a) Scan rate-normalized anodic current ($i/v^{1/2}$) at 0.1 V as a function of $v^{1/2}$. The linear behavior between $i/v^{1/2}$ and $v^{1/2}$ indicates the pseudocapacitive nature of the active electrode material. (b) Relative contributions of the diffusive and capacitive currents to the CV curves at different scan rates. (c, e) CV response for the pristine WO_3 electrode at 5 mV s^{-1} and 80 mV s^{-1}, respectively. (d, f) CV response for the NFA-embedded WO_3 electrode at 5 mV s^{-1} and 80 mV s^{-1}, respectively. The shaded region represents the capacitive contribution to the total current.

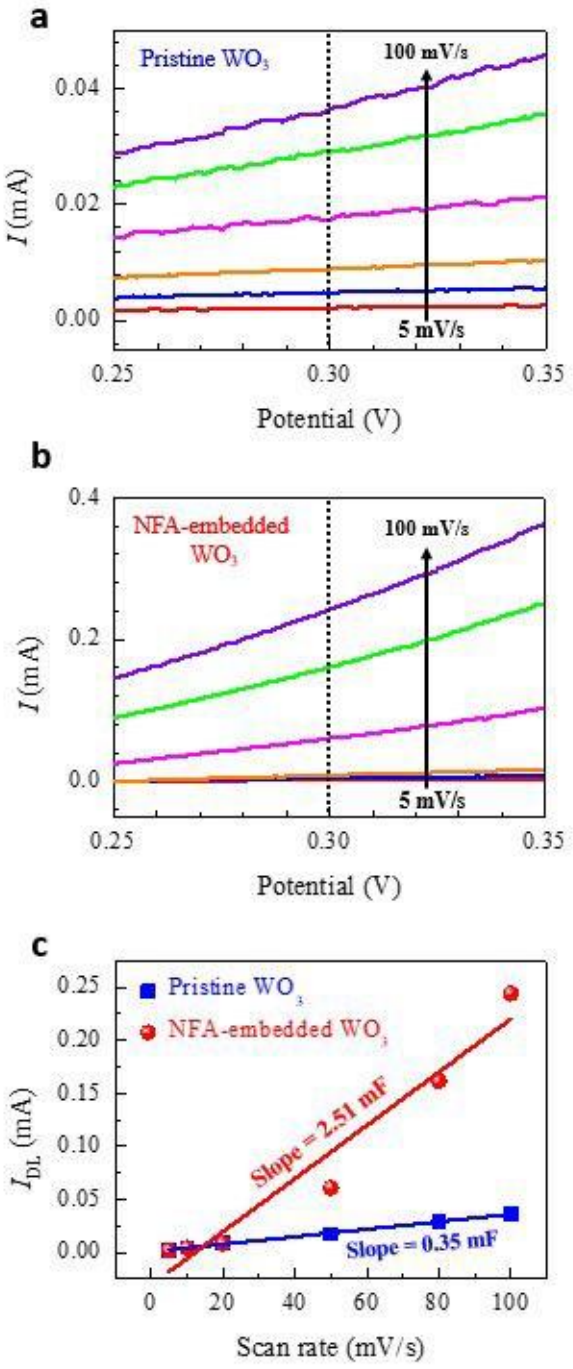

Fig. 4 (a, b) CV curves of the pristine WO_3 and NFA-embedded WO_3 electrodes at different scan rates in the nonfaradaic voltage region. (c) Nonfaradaic current density from the CV curves at 0.3 V as a function of the scan rate (mV s^{-1}). The slope corresponds to the double-layer-region specific capacitance.

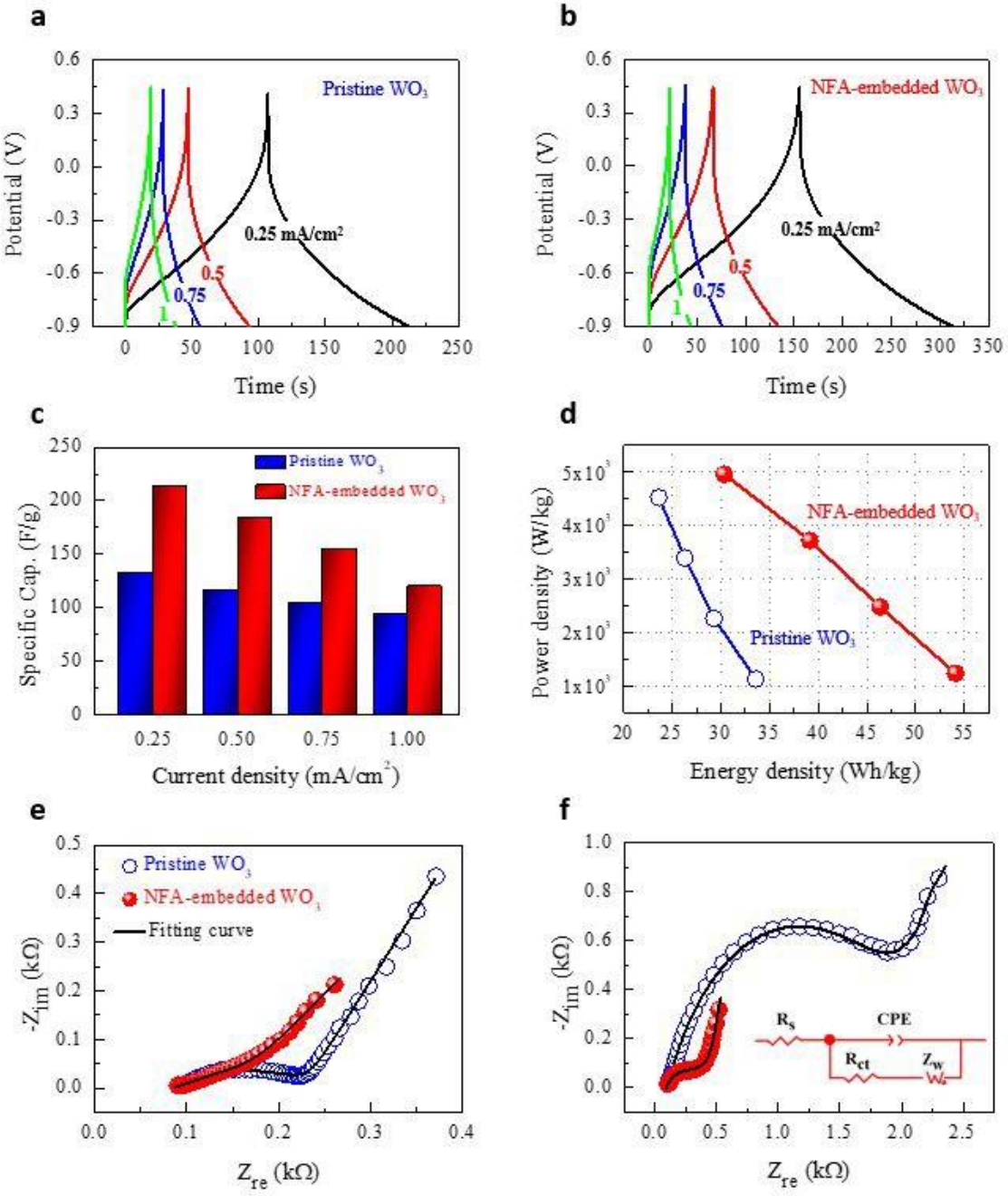

Fig. 5 (a, b) GCD curves at different current densities for the pristine WO_3 and NFA-embedded WO_3 electrodes, respectively. (c) Comparison of the specific capacitance measured at different current densities. (d) Ragone plot describing the relation between the measured specific power and the specific energy. Impedance spectra (Nyquist plots) of the pristine WO_3 and NFA-embedded WO_3 electrodes (e) before and (f) after 2000 cycles. The inset shows the equivalent circuit diagram.

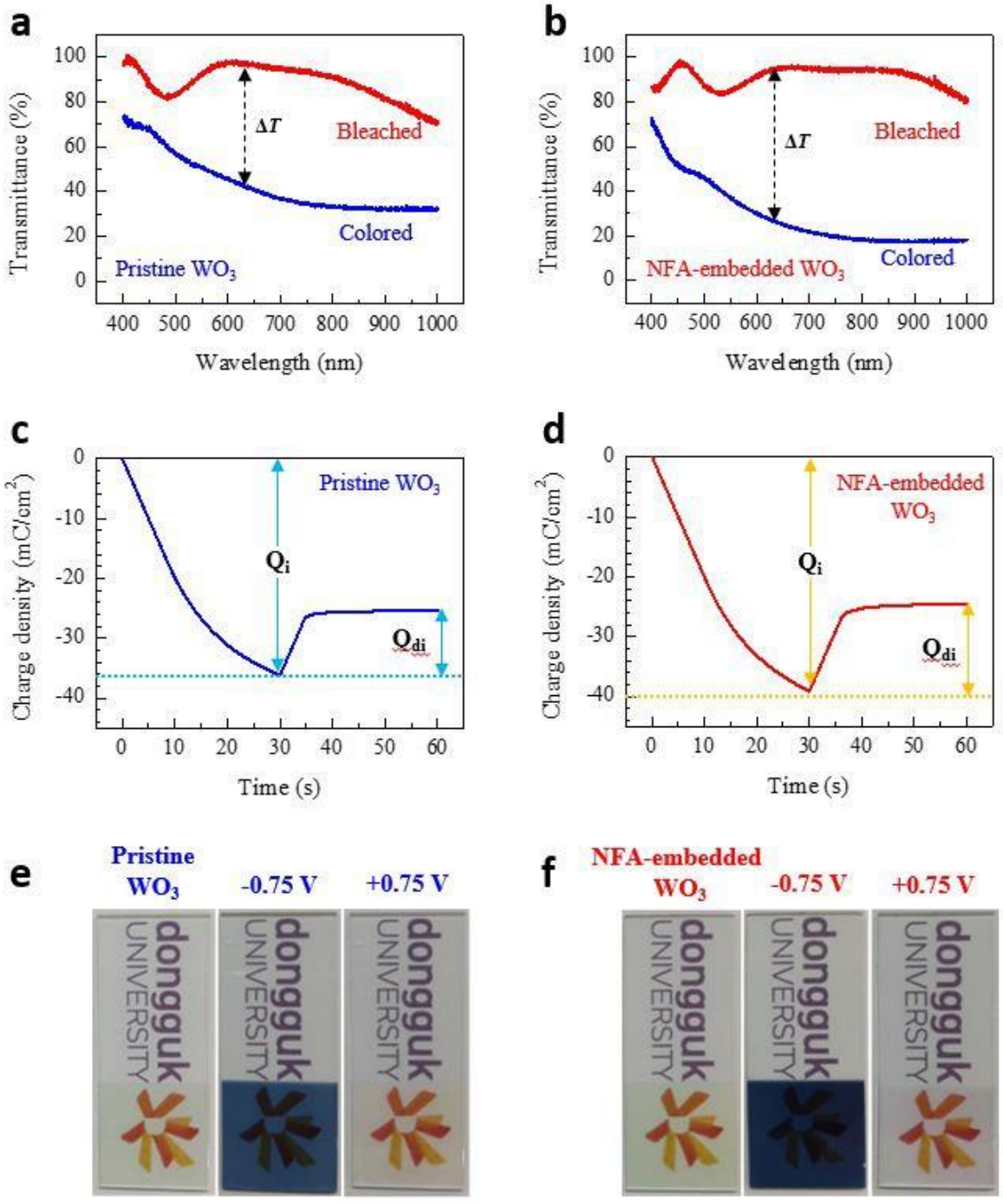

Fig. 6 (a, b) Transmittance spectra of the pristine WO_3 and NFA-embedded WO_3 electrodes at the colored and bleached states, respectively. $\Delta T = T_b - T_c$ at a wavelength of 630 nm. (c, d) Chronocoulometry curves of the pristine WO_3 and NFA-embedded WO_3 electrodes, respectively. (e, f) Photos of the pristine WO_3 and NFA-embedded WO_3 electrodes at the colored (−0.75 V) and bleached (+0.75 V) states. The visual color indicates the level of energy stored in the electrode.

Table 1 Extracted circuit parameters obtained by modelling the recorded EIS curves.

	Before cycling				After 2000 cycles			
	R_s (Ω)	R_{ct} (Ω)	CPE (μF)	Z_w (Ω)	R_s (Ω)	R_{ct} (Ω)	CPE (μF)	Z_w (Ω)
Pristine WO_3	93	120.5	74	60.2	105.7	1970	37.0	2950
NFA-embedded WO_3	80	5.5	100	230.7	91.9	247	361.5	386

Table 2 Comparison of electrochromic performance parameters of the pristine WO_3 and NFA-embedded WO_3 electrodes.

	Q_i (mC/cm^2)	Q_{di} (mC/cm^2)	Reversibility (%)	Transmittance (%)		Optical modulation (%)	Optical density (ΔOD)	Coloration efficiency (cm^2/C)
				T_b	T_c			
Pristine WO_3	-36.17	10.84	29.96	97.13	42.47	54.65	0.82	91.46
NFA-embedded WO_3	-39.10	14.58	37.28	94.51	27.01	67.49	1.25	128.10

Table of content

Nanofilament array embedded metal oxide for a highly efficient electrochemical electrode

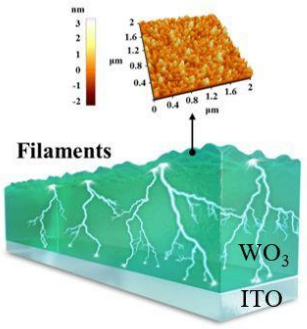

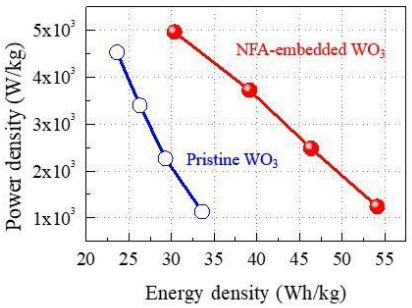

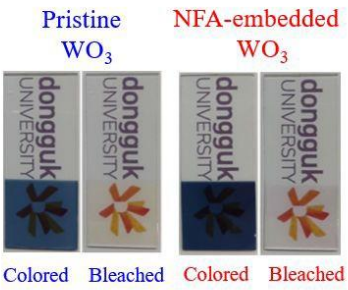

Supporting Information

Nanofilament array embedded tungsten oxide for highly efficient electrochromic supercapacitor electrodes

Jongmin Kim,[a] Akbar I. Inamdar ,[a] Yongcheol Jo,[a] Sangeun Cho,[a] Abu Talha Aqueel Ahmed,[a] Bo Hou,[b] SeungNam Cha,[c] Tae Geun Kim,[d] Hyungsang Kim*,[a] & Hyunsik Im*,[a]

[a] *Division of Physics and Semiconductor Science, Dongguk University, Seoul 04620, South Korea*
[b] *Department of Engineering Science, University of Cambridge, Cambridge, CB2 1TN, UK*
[c] *Department of Physics, Sungkyunkwan University, Suwon, 16419, Republic of Korea*
[d] *Department of Electrical Engineering, Korea University, Seoul 02841, South Korea*

** Corresponding authors: hskim@dongguk.edu, hyunsik7@dongguk.edu*

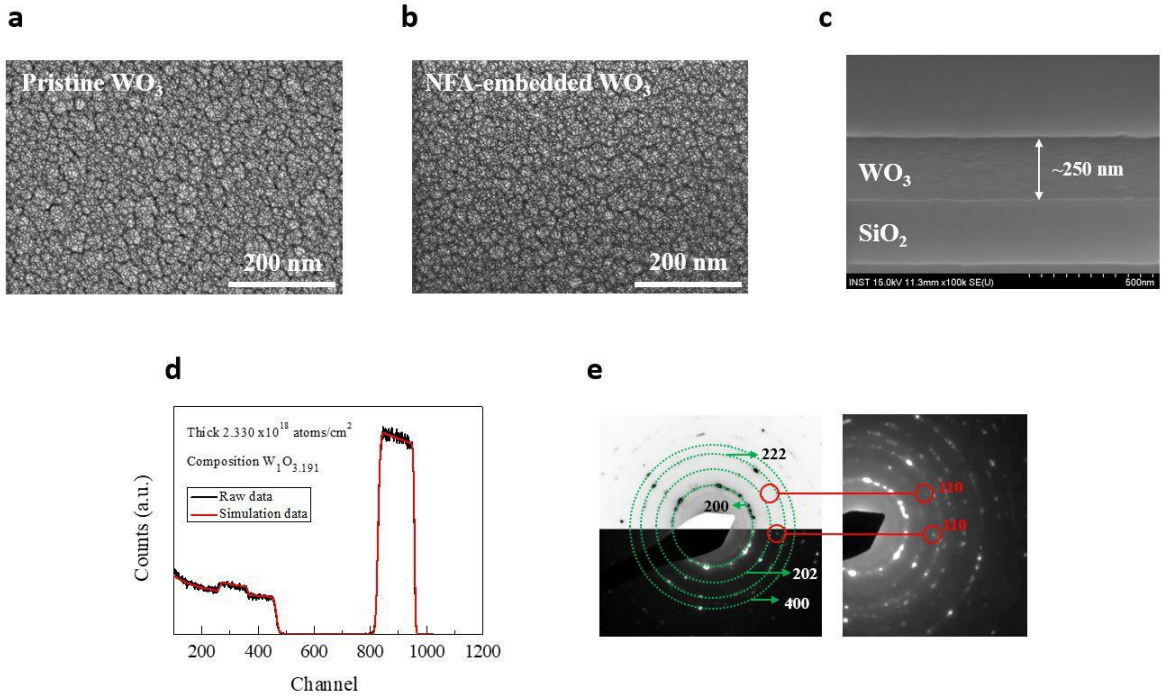

Fig. S1 Top-view field-emission scanning electron microscopy (FE-SEM) images for (a) the pristine WO_3 and (b) NFA-embedded WO_3 films. (c) Cross-sectional FE-SEM image of the WO_3 film. FE-SEM image showing the thickness of the WO_3 film. (d) Rutherford backscattering spectroscopy (RBS) profiles of the WO_3 film. (e) SAED patterns measured after the electroforming process.

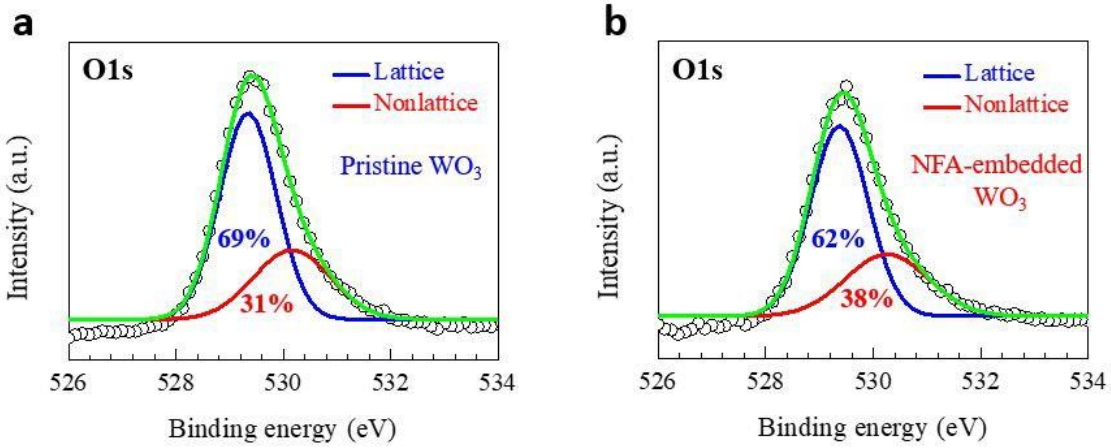

Fig. S2 XPS spectra for O1s peaks in (a) the pristine WO_3 and (b) NFA-embedded WO_3 films.

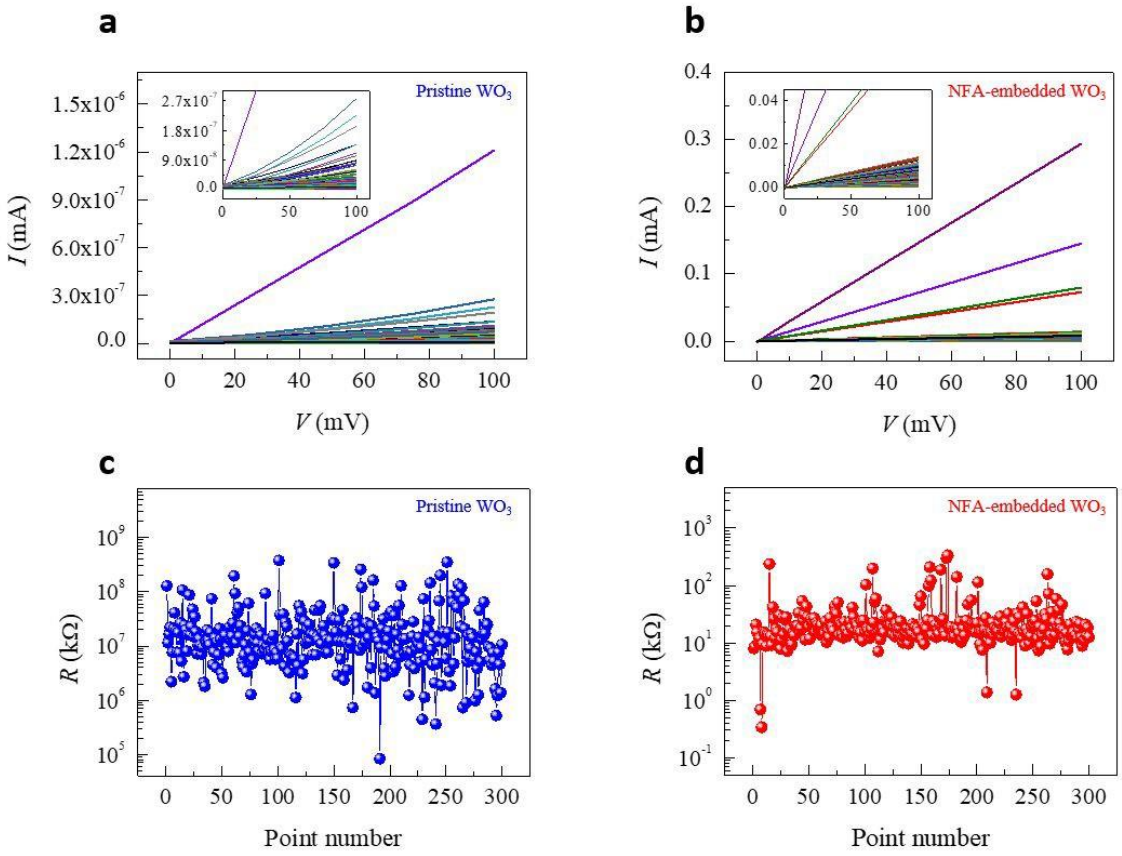

Fig. S3 Two-probe *I-V* characteristics with contacts the WO_3 film and the conducting ITO substrate. (a, b) The measured *I-V* curves for the pristine WO_3 and NFA-embedded WO_3 electrodes. The insets show magnified views of the *I-V* curves. (c, d) The resistance as a function of the point number at 0.1 V read voltage. The resistance ratio between the pristine WO_3 and NFA-embedded WO_3 electrodes more than 6 orders of magnitude.

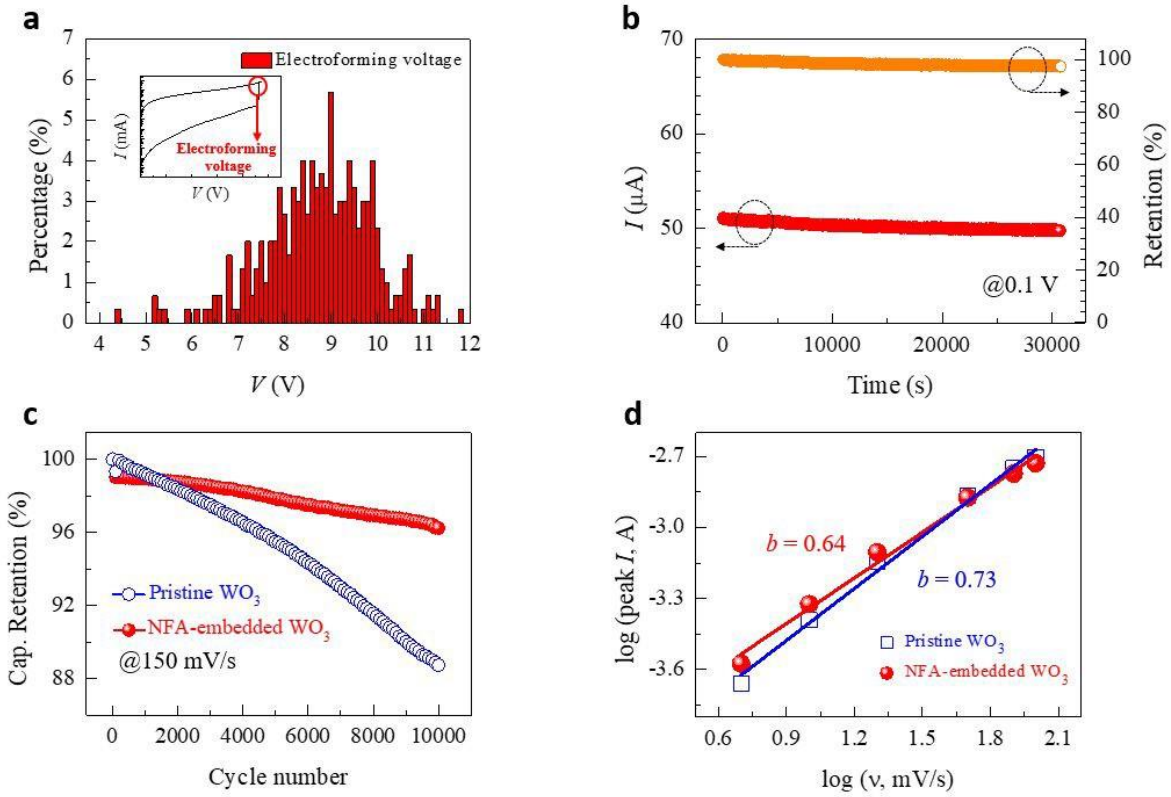

Fig. S4 (a) Distribution of electroforming voltage for the NFA-embedded WO_3 electrode. The inset shows the electroforming voltage. (b) Retention characteristic of the NFA-embedded WO_3 electrode at room temperature and 0.1 V read voltage with almost stable current value. (c) Cycling performance for 10000 cycles at a scan rate of 150 mV s^{-1}. (d) Determination of the *b*-value at scan rates from 5 to 100 mV s^{-1}.

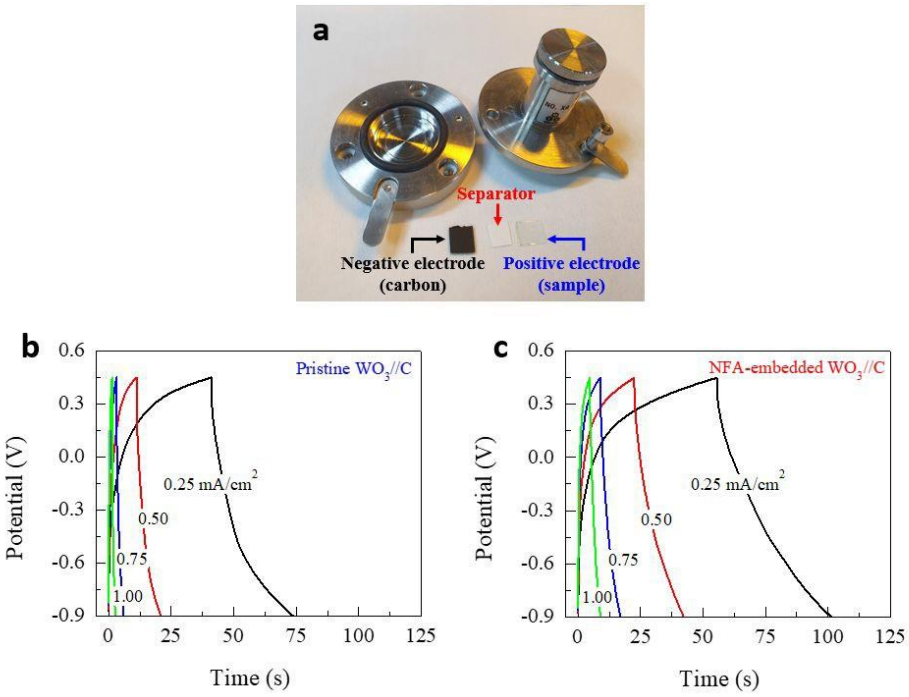

Fig. S5 (a) Photograph showing the asymmetric supercapacitor. The galvanostatic charge–discharge profiles of (b) the pristine WO_3//C and (c) NFA-embedded WO_3//C asymmetric supercapacitor devices at various current densities.

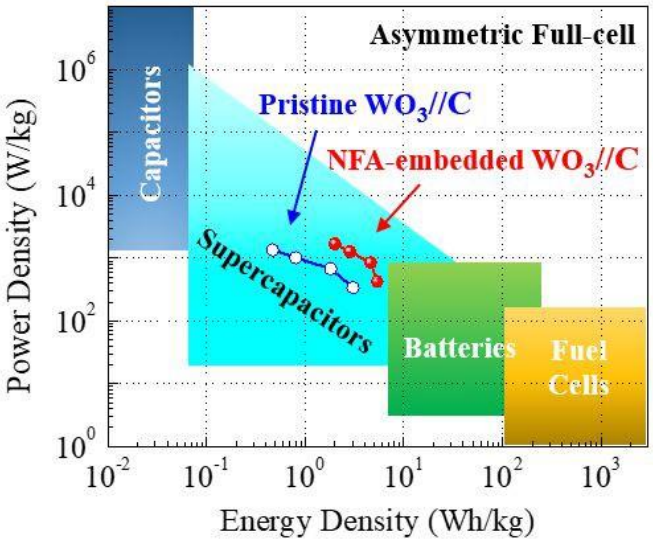

Fig. S6 Energy density vs. power density for the pristine WO_3//C and NFA-embedded WO_3//C asymmetric supercapacitors.

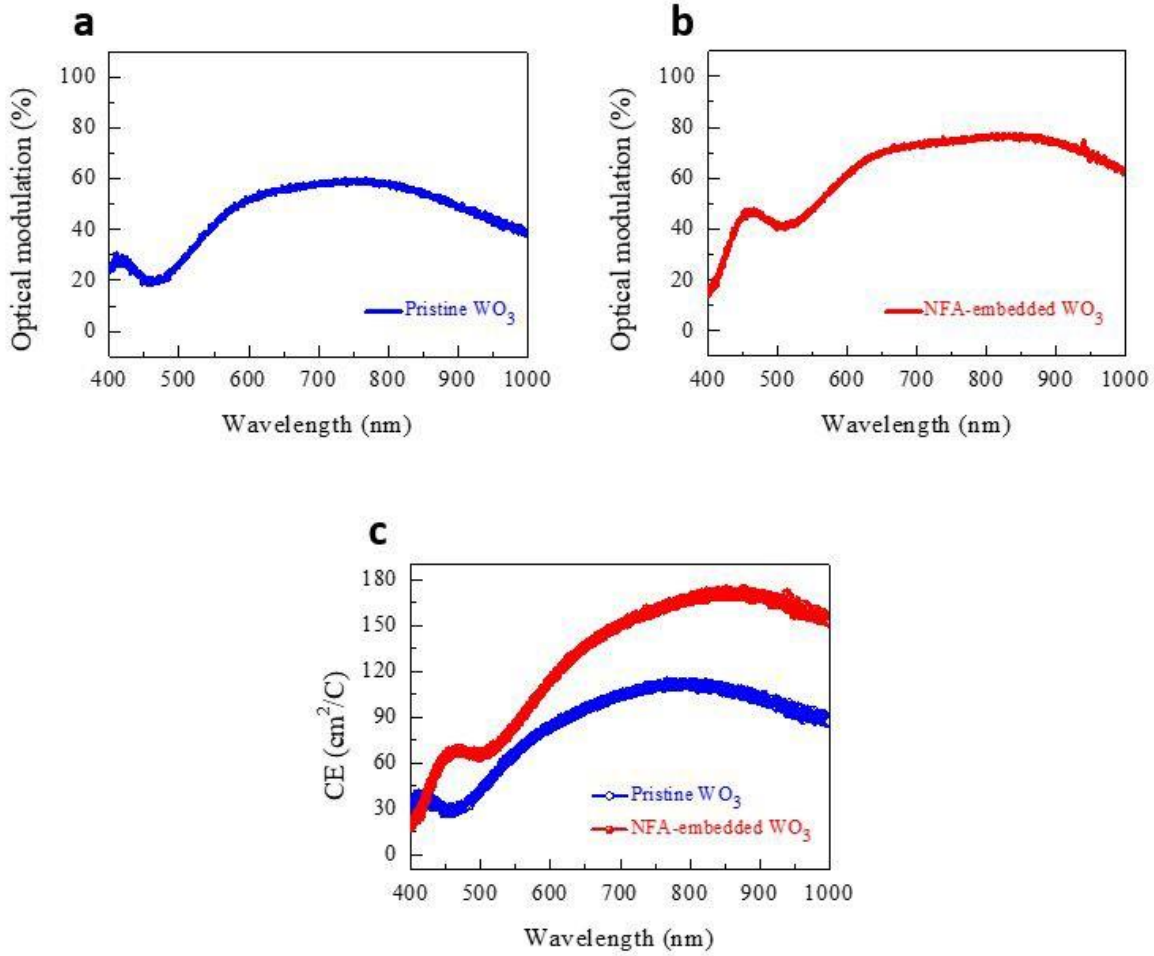

Fig. S7 (a, b) Optical modulation and (c) coloration efficiency for the pristine WO_3 and NFA-embedded WO_3 electrodes.

Table S1 Percentages of different chemical states of W for pristine WO_3 and NFA-embedded WO_3 films.

	Percentages of chemical states of W (%)	
Chemical states	Pristine WO_3	NFA-embedded WO_3
W^0 (Metallic W)	0	12.3
W^{4+} (WO_2)	0	33.6
W^{5+} (W_2O_5)	32.2	10.9
W^{6+} (WO_3)	67.8	43.2